Catalysis Today 267 (2016) 28–40

Contents lists available at ScienceDirect

Catalysis Today

journal homepage: www.elsevier.com/locate/cattod

Ab initio X-ray absorption modeling of Cu-SAPO-34: Characterization of Cu exchange sites under different conditions

Renqin Zhang[a], Kathy Helling[a], Jean-Sabin McEwen[a,b,c,*]

[a] The Gene and Linda Voiland School of Chemical Engineering and Bioengineering, Washington State University, WA 99164, United States
[b] Department of Physics and Astronomy, Washington State University, WA 99164, United States
[c] Department of Chemistry, Washington State University, WA 99164, United States

ARTICLE INFO

Article history:
Received 7 October 2015
Received in revised form
12 December 2015
Accepted 4 January 2016
Available online 29 March 2016

Keywords:
Copper
Density functional theory
Zeolite
SAPO-34
XANES

ABSTRACT

Copper-exchanged SAPO-34 (Cu-SAPO-34) provides excellent catalytic activity and hydrothermal stability in the selective catalytic reduction (SCR) of NO_x by using NH_3 as a reductant. We find that the 6-membered ring (6MR) site is the most energetically favorable for a Cu^+ ion while the 8-membered ring (8MR) sites are less favorable by about 0.5 eV with respect to the 6MR site in Cu-SAPO-34. Upon adsorption of molecular species (H_2O, O, OH, O_2), the energy differences between Cu in the 8MR and 6MR sites decreases and almost disappears. Further, a thermodynamic phase diagram study shows that a Cu^+ ion bound to a single H_2O molecule is the most stable species at low oxygen potential values while a Cu^{2+} ion bound to 2 OH species is more stable when the oxygen chemical potential is sufficiently high. By comparing Cu K-edge XANES between Cu-SSZ-13 and Cu-SAPO-34 with Cu in different oxidation states, we conclude that it is difficult to differentiate the simulated XANES of Cu in these structures at a given oxidation state. By studying the Cu K-edge XANES of several favorable structures in Cu-SAPO-34 in the presence of adspecies, the simulated XANES results capture the real trend of the edge shift with oxidation state and gives new insights into the experimentally determined XANES of Cu-SAPO-34 obtained under standard SCR conditions.

1. Introduction

Copper-exchanged silicoaluminophosphate (Cu-SAPO-34) has drawn extensive attention as a catalyst for selective catalytic reduction (SCR) of NO_x with an NH_3 reductant. Cu-SAPO-34 and copper-exchanged aluminosilicate (Cu-SSZ-13) are structurally analogous chabazite zeolites, which have excellent hydrothermal durability [1–3]. SAPO-34 molecular sieves are synthesized using various structure directing agents (or templates), such as morpholine (MA), triethylamine (TEA), diethylamine (DEA), tetraethylammonium hydroxide (TEAOH) or a mixture of them [4,5]. Recent results have shown that the template affects the Si coordination structures in SAPO-34, and that the Si coordination structures further adjust the acid properties and the Cu species distribution on the Cu-SAPO-34 catalyst [5]. They concluded that with the same Si content, the Cu/TEA and Cu/TEAOH samples contain less Cu^{2+} species and more CuO species than the Cu/MA and Cu/DEA samples due to the existence of a Si island. It is reported that Cu-SAPO-34 samples are more insensitive to hydrothermal aging than Cu-SSZ-13 [6]. Furthermore, high-temperature aging is found to improve the catalytic performance of Cu-SAPO-34 due to the migration of Cu species in the fresh sample from the external surface into the micropores [3,4,7,8] and the formation of isolated Cu ions at the exchange sites during the aging process [3]. It is also reported that migration of Cu species from the surface upon activation of Cu-SAPO-34 leads to a several-fold increase in catalytic activity for the selective catalytic reduction (SCR) of NO_x with NH_3 as a reductant [7].

By utilizing different experimental techniques, isolated Cu^{2+} species in Cu-SAPO-34 were found to be the active sites of NH_3-SCR [3,9–12]. For the relationship between Cu species and Cu loading in Cu-SAPO-34, similar to Cu-SSZ-13 [13], it was reported that the amount of isolated Cu^{2+} increased with increasing Cu loading up to 2.0 wt% and only slightly increased with higher Cu loading [9,12]. An increase in the amount of the isolated Cu^{2+} caused the improvement of the NH_3-SCR activity and a decrease in the amount of CuO induced a decline in the NH_3 oxidation activity [14]. However, the amount of Cu_xO_y clusters continuously increased at higher Cu loading. The presence of Cu_xO_y may promote NH_3 oxi-

* Corresponding author at: The Gene and Linda Voiland School of Chemical Engineering and Bioengineering, Washington State University, WA 99164, United States.
E-mail address: js.mcewen@wsu.edu (J.-S. McEwen).

http://dx.doi.org/10.1016/j.cattod.2016.01.025
0920-5861/

dation by O_2, leading to the observed decrease in standard SCR performance at high temperatures [9] where the competing NH_3 oxidation decreases the SCR activity [10]. It was found that the turnover frequency calculated based on the number of isolated Cu^{2+} ions in samples with varying Cu loading showed a constant value at the same temperature [12]. Based on these results, it was concluded that the isolated Cu^{2+} species is the active site for the NH_3-SCR reaction over a Cu-SAPO-34 catalyst. As opposed to Cu-SSZ-13 [15], the Brønsted acid sites in Cu-SAPO-34, act as an NH_3 reservoir rather than being directly involved in the SCR reaction [10,16]. A key step in the proposed mechanism is the formation of surface nitrates and nitrites, which react with NH_3 to form NH_4NO_2 and NH_4NO_3 [16]. By performing the electron paramagnetic resonance (EPR) experiments, Yu et al. also proved that the isolated Cu^{2+} species are the active sites and the NH_4NO_2 species is the intermediate for NH_3-SCR over Cu-SAPO-34 [10]. In addition, NH_3-SCR over Cu-SAPO-34 presents a different mechanism at low and high temperatures [17]. At low temperatures, NH_4NO_3 is a key intermediate while at high temperatures, NO_2 is an important intermediate and NH_3 oxidation is competitive with NH_3-SCR. They observed a double peak shape with a dip point at the approximately moderate temperature of 390 °C [17,18].

Currently, some issues still need to be addressed for CHA-based SCR catalysts such as the unclear effect of reactants on the Cu location and reaction mechanism. Experimental evidence has demonstrated that Cu ions are the active sites for NH_3-SCR reactions [5,8–11]. However, the location of Cu ions in Cu-SSZ-13 zeolite is still unclear. Understanding the catalytic properties of Cu-SAPO-34 at the atomic and electronic level is important. However, there are few theoretical studies on the properties of Cu-SAPO-34 [19–22]. These studies help us to understand better the locations of Cu ions and molecular adsorption behaviors on the active sites. It has been reported that higher Cu loadings can result in the formation of Cu_xO_y clusters [9,12]. In the Cu-SAPO-34 zeolite, Cu is located in 8-membered ring and has two facets where it can interact with reactants while Cu located in the 6-membered ring can only interact from one side. It also appears that the Cu species may relocate under reaction conditions. In order to use Cu-SSZ-13 and Cu-SAPO-34 optimally and further develop Cu-based zeolite catalysts, the differences between the Cu-SSZ-13 and Cu-SAPO-34 were discussed in the literature [6,8,17]. In all SCR performance tests, NH_3 oxidation and characterization results consistently indicate that Cu-SAPO-34 is more robust than Cu-SSZ-13 toward hydrothermal aging temperatures higher than 800 °C [6,8]. Activity tests indicated that the Cu-SAPO-34 catalyst had a relatively higher deNO_x performance than the Cu-SSZ-13 catalyst [17]. As a continuation of our work in understanding the properties of Cu-exchanged CHA zeolite catalyst [23,24], the catalytic properties of Cu-SAPO-34 are investigated by using calculations from first-principles. Further, by using *operando* XAS, it has been confirmed that Cu^+ was present under standard SCR reaction conditions over a Cu-SAPO-34 catalyst [25], as shown in Fig. 1. It also demonstrates the importance of performing *operando* experiments and how *in situ* XANES may lead to the incorrect determination of the steady state structure. We will look at several structures and assign the Cu^+ peak by examining Cu K-edge XANES of various Cu^+ species. In this contribution we will study the adsorption of O, O_2, OH, and H_2O on a Cu ion in Cu-SAPO-34. We will simulate the corresponding Cu K-edge XANES as well as compare the multiple possible Cu positions through density functional theory (DFT) calculations so as to gain insights into the underlying experimental XANES spectrum measured under standard SCR conditions.

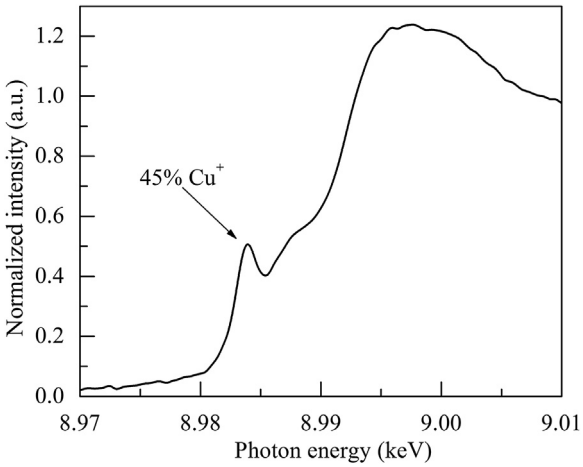

Fig. 1. Normalized XANES spectrum of a commercial ~1.75 wt% Cu-SAPO-34 catalyst collected in *operando* reactor (solid line) while feeding a standard SCR mixture (300 ppm NO, 300 ppm NH_3, 5% O_2, 5% H_2O, 5% CO_2 and balance heat 200 °C) [25]. It is identified that the amount of Cu^+ is 45% in the mixture of Cu ions.

2. Computational details

DFT calculations were performed with the Vienna *Ab initio* Simulation Package (VASP) code [26,27]. The projector augmented-wave (PAW) [28,29] method and the generalized-gradient approximation (GGA), using the PW91 functional [30], were employed for the treatment of the electron-ion interactions and the exchange-correlation effects, respectively. With its PAW potentials, VASP combines the accuracy of all-electron methods with the computational efficiency of plane-wave approaches. The total energy convergence threshold was set to 10^{-8} eV and the geometries were considered to be fully relaxed when the forces were less than 0.01 eV/Å.

As is well known, the Cu-SAPO-34 zeolite belongs to the chabazite structure which is composed of 4-membered rings (4MR), 6-membered rings (6MR), and 8-membered rings (8MR). As shown in Fig. 2, in the pure aluminophosphate ALPO-34, the Al and P atoms on tetrahedral sites (T) obey strictly alternated ordering and there are four nonequivalent O sites, which can be distinguished according to their participation in different rings of the framework. Further information can be found in our previous paper on Cu-SSZ-13 [24]. The calculations in this contribution were performed in a rhombohedral unit cell, consisting of 12 T atoms and 24 O atoms. Monovalent Cu-exchanged SAPO-34 (ZCu) is produced by replacing one Si atom with one P atom and using Cu to compensate the charge deficit. Cu^{2+}-SAPO-34 (Z_2Cu) is generated by the replacement of two P atoms with two Si atoms, where the Cu ion presents the oxidation state of 2+. Structures of ALPO-34 and Cu-SAPO-34 were firstly relaxed to obtain the equilibrium volumes. For the pure ALPO-34, an equilibrium rhombohedral volume of 844.8 $Å^3$ was obtained which is consistent with the results of 829.6 $Å^3$ and 831.9 $Å^3$ as reported in the literature [20,31]. With the replacement of a P atom with a Si atom and an exchanged a Cu atom, the calculated equilibrium volume of ZCu is 847.4 $Å^3$ (see Fig. S1 in Supplementary Information), which is slightly larger than that of ALPO-34. However, with the replacement of two P atoms with two Si atom and an exchanged a Cu atom, the equilibrium volume of Z_2Cu is 840.8 $Å^3$ (see Fig. S1 in Supplementary Information), which is slightly smaller than that of ALPO-34. In this contribution, we start our study on ZCu with the adsorption of adspecies (O, OH and H_2O) with different oxidizing power. The 'oxidizing power' refers to the ability to oxidize the Cu^+ ion into a higher oxidation state. In another words, the 'oxidizing power' refers to the ability of the adspecies to obtain electrons from Cu ion. When a neutral

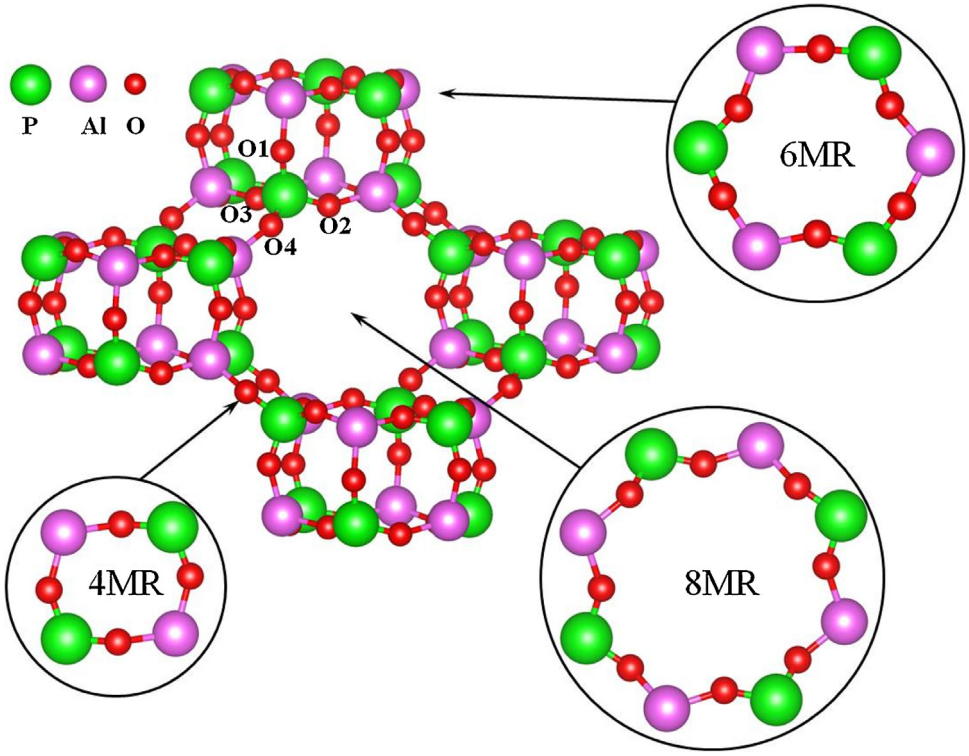

Fig. 2. Chabazite structure of ALPO-34, and the compositions of 4MR, 6MR and 8MR are shown. The four nonequivalent O sites are labeled in a P tetrahedral structure. Same distribution of O sites is applied to Al tetrahedral structures. Green, pink and red spheres represent P, Al and O atoms, respectively.

OH (or O) attaches onto the Cu^+ ion in ZCu, an electron transfers from the Cu ion to the OH (or O) species, whereby a $[Cu^{2+}(OH)^-]^+$ (or $[Cu^{2+}(O^-)]^+$) forms. It is reported that the Cu ions can have different oxidation states between +1 and +2 during the SCR process [10].

The Cu binding energy is calculated by

$$E_b = E_{ZCu} - E_{SAPO-34} - E_{bulk}^{Cu} \quad (1)$$

where E_{ZCu} , $E_{SAPO\text{-}34}$ and E_{bulk}^{Cu} are the total energies of ZCu, ZCu with removing Cu, and bulk Cu, respectively.

For the molecular adsorption calculations, the unit cell of H_2O adsorbed in the ZCu conformation was fully relaxed using the step by step procedure indicated in Supplementary Information section. Comparing with clean ZCu, the adsorption of H_2O slightly increases the equilibrium volume to 850.1 $Å^3$. The plot of the energy as function of volume can be found in Fig. S1 of Supplementary Information. Other adsorbates were studied in the unit cell using the lattice constants identified for H_2O adsorbed on ZCu. A 400 eV plane-wave cutoff and a single Γ-point sampling of the Brillouin zone was used for these calculations. Adsorption energies E_{ads} are calculated by the following equation:

$$E_{ads} = E_{tot} - E_{ZCu} - E_{mol} \quad (2)$$

where E_{tot}, E_{ZCu}, and E_{mol} are the total energies of ZCu with molecular adsorption, clean ZCu, and the isolated molecules in gas phase, respectively. We note that although the PW91 functional is appropriate for the work done in this contribution, it does not account for the vdW interactions and would not be suitable to determine accurate adsorption energies [32].

The calculations of the theoretical K-edge XANES of Cu in Cu-SSZ-13 were carried out using the CASTEP code [33]. Here we simulated the X-ray spectra through the calculation of the electron energy loss spectra (EELS) [34]. EELS and XANES are identical in principle. In order to avoid confusion, we use the term of theoretical XANES in this contribution. CASTEP is a density functional theory code that uses a plane wave basis sets and ultrasoft pseudopotentials. Note that the calculations of the XANES spectra were not affected whether or not one optimized the unit cell within CASTEP (see details in Fig. S2). As a result, the unit cell in CASTEP was fixed to the unit cell as optimized by the VASP program. The GGA-PBE [35] exchange correlation functional was used in these calculations for the optimization of the atomic coordinates using the fixed unit cell geometry and for the simulation of the XANES. We remark that although the PBE, RPBE, or PBEsol functionals are recommended when a GGA functional is required for such calculations, we found that the results of theoretical K-edge XANES of Cu in ZCu with Cu in 6MR site are independent of such exchange-correlation functionals [24]. To calculate the XANES spectra, ultrasoft pseudopotentials were generated on the fly [34], and one core electron was excited from a relevant core level when performing core-hole calculations. It is demonstrated that the core-hole effect is significant on the results of core level spectra [36]. Therefore, we took into account the core-hole effect in our calculations. All core-hole calculations were carried out using supercells sufficiently large so as to eliminate the interactions between periodic images. Previous work recommends a distance between images of 8–10 Å [34,37]. The dimensions of the rhombohedral unit cell used in our calculations satisfy this requirement. Energy cutoffs of 550 eV and a K-point grid of $(5 \times 5 \times 5)$ were used in the calculations of the XANES. The energy broadening with an instrumental smearing, using the Gaussian method, of 0.6 eV and lifetime broadening of Cu with a value of 1.55 eV were applied [34].

3. Results and discussions

3.1. Pure ALPO-34 and clean SSZ-13

Both SSZ-13 and ALPO-34 belong to the chabazite (CHA) structure. Their difference lies in the tetrahedral sites occupied by a Si atom for SSZ-13 whereas Al and P atoms in ALPO-34 occupy these sites. It is reported that this structural difference causes the dif-

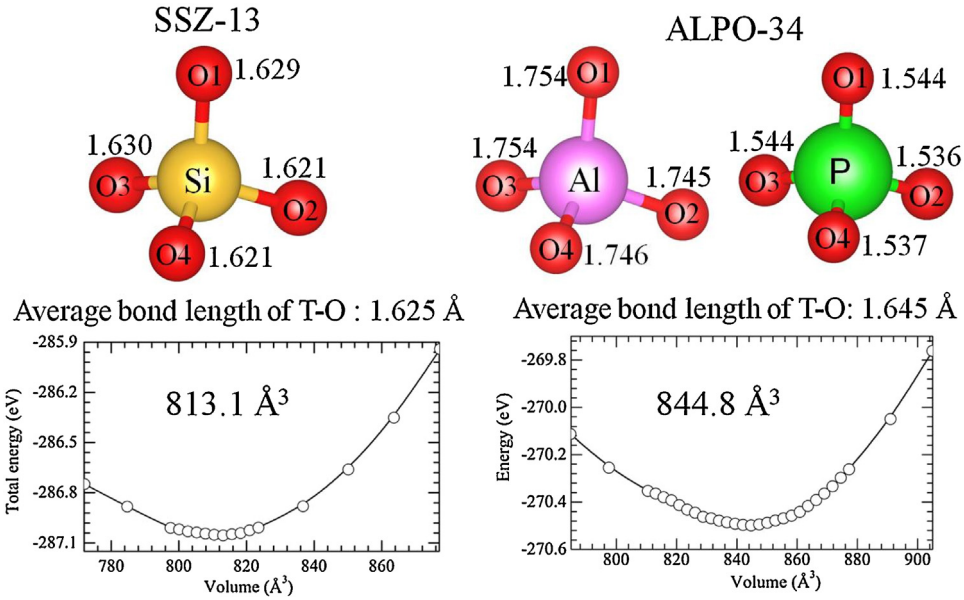

Fig. 3. The tetrahedral structure in pure SSZ-13 and ALPO-34 are shown as well as plots of total energy as function of volume. The bond lengths of T—O bond are presented.

ferent mechanisms for dealumination of SSZ-13 and desilication of SAPO-34 [38]. Regarding their equilibrium volumes, which are 813.1 Å^3 for SSZ-13 and 844.8 Å^3 for ALPO-34, ALPO-34 is larger than SSZ-13. The chabazite volume is determined by the tetrahedral structure. Fig. 3 shows the tetrahedral structures of Si, Al and P atoms in SSZ-13 and ALPO-34, respectively. It is found that the bond length of Si—O is longer than P—O while shorter than Al—O. The average T—O bond lengths are 1.625 Å for SSZ-13 and 1.645 Å for ALPO-34, which results in the equilibrium volume of ALPO-34 being larger than that of SSZ-13. When one replaces Si with P in ALPO-34, the equilibrium volume will also vary and thus needs to be taken into account in our calculations. As mentioned before, the resulting equilibrium volumes that were used when one replaces one P atom with one Si atom or two P atoms with two Si atoms are given in Supplementary Information.

3.2. Locations of Cu ion in clean ZCu

Three possible positions of Cu in ZCu are considered in this contribution. One is located in the center of the 6MR and the other two are in the 8MR sites distinguished by forming bonds with different O atoms. We note that there is not enough room for Cu in the 4MR site, and this option was not investigated in this contribution. As shown in Fig. 4, for the two positions of Cu in the 8MR sites, Cu atoms are bonded with the O1 and O4 atoms or the O2 and O4 atoms of the zeolite framework, and the resulting structures are called 8MR_O14 and 8MR_O24, respectively.

As shown in Fig. 4, it was found that Cu in the 6MR site has a 3-fold coordination to O atoms. For the 6MR site, Cu is bonded to an activated O3 atom to form the smallest Cu—O bond length of 1.944 Å, and two non-activated O3 atoms with longer Cu—O bond lengths of 2.008 and 2.306 Å, respectively. This finding is consistent with other computational results in the literature [19]. Here we denote an activated O atom as one that is bonded to an adjacent Si atom. When Cu is in the 8MR_O14 site it is bonded with the activated O1 and O4 atoms. The Cu ion is also close to a non-activated O2 atom with a distance of 2.353 Å. We used the differential charge density to investigate if the Cu ion and O2 atom form a bond. As shown in Fig. S3 in Supplementary Information, there is no sharing of electrons between the Cu ion and O2 atom. It is thus concluded that Cu in 8MR_O14 site has a coordination number of two. The Cu 8MR_O24 site is 2-fold coordinated with activated O2 and O4 atoms, where the Cu—O bond lengths are 2.026 and 2.058 Å. We therefore conclude that the coordination number of Cu in the 6MR site is 3 while that of the Cu in the two 8MR sites is 2.

Comparing the properties of Cu in different positions, it was found that the 6MR site is the most thermodynamically favorable. The configurations of Cu in the 8MR_O14 and 8MR_O24 sites are slightly less favorable with total energy differences of 0.50 and 0.52 eV, respectively, with respect to that of Cu in 6MR site. Based on the results of the Cu binding energy, Cu in the 6MR site has a stronger electrostatic interaction with the CHA framework. The Cu binding energies are −0.88, −0.38 and −0.32 eV for Cu in the 6MR, 8MR_O14 and 8MR_O24 sites, respectively. We conclude that the 6MR site is the primary site for Cu to occupy while the 8MR sites are the second most favorable sites where Cu ions can be located. These results support the experimental results that there are two different types of Cu present in the SAPO-34 zeolite [39]. Specifically, Cu ions primarily occupy sites in the 6MR at low Cu loading, while at high Cu loading some Cu ions are located in the large CHA cages and close to the 8MR sites.

3.3. Molecular adsorption on ZCu

The most common and abundant reactive gases under SCR conditions are O_2 and H_2O, and understanding the interactions of Cu centers with these gases and their decomposition products is central to understanding the nature, oxidation state, and redox activity of these materials. We take a general approach and consider the adsorption of various species of H_2O, OH, O, O_2 and 2OH to a Cu center.

An O^- species is the simplest possible adsorbate intermediate under SCR oxidative conditions, and Fig. 5 shows the relaxed structure for $[Cu^{2+}(O^-)]^+$ in the 6MR, 8MR_O14 and 8MR_O24 sites. The O^- species draws the Cu ion out of the plane of the 6MR into a location above the 6MR. With the formation of $[Cu^{2+}(O^-)]^+$, the Cu^{2+} is coordinated to the two activated O atoms and the adsorbed O^-, which results in a net 3-fold coordination of Cu^{2+} in different locations (6MR and 8MR sites). The Cu—O bond length of Cu formed with lattice O is about 2.0 Å while that of Cu formed with adsorbed O^- is about 1.7 Å. As mentioned previously, the configuration of Cu in the 6MR is the most favorable for clean ZCu. However, as

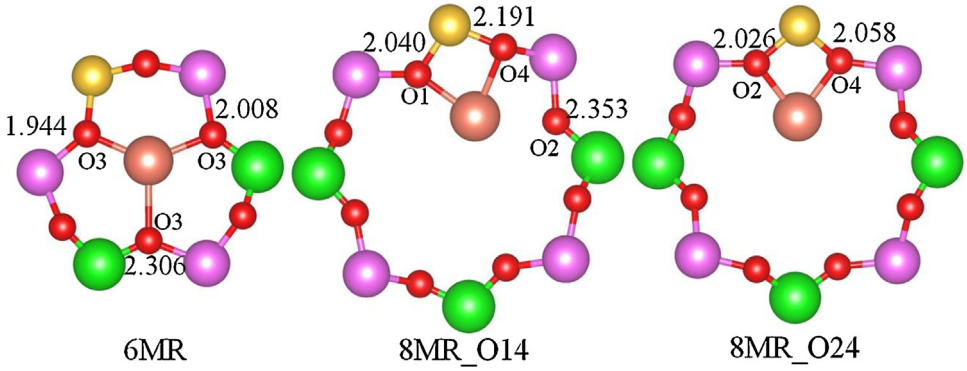

Fig. 4. Local structures of three possible Cu positions (6MR, 8MR_O14 and 8MR_O24) in ZCu. Cu—O distances with unit of Å are indicated in each panel. The atoms represented are the same as previous figures. The different O atoms are labeled as presented in Fig. 2. Please note that these shown structures are portion of the periodic structure of the rhombohedral unit cell.

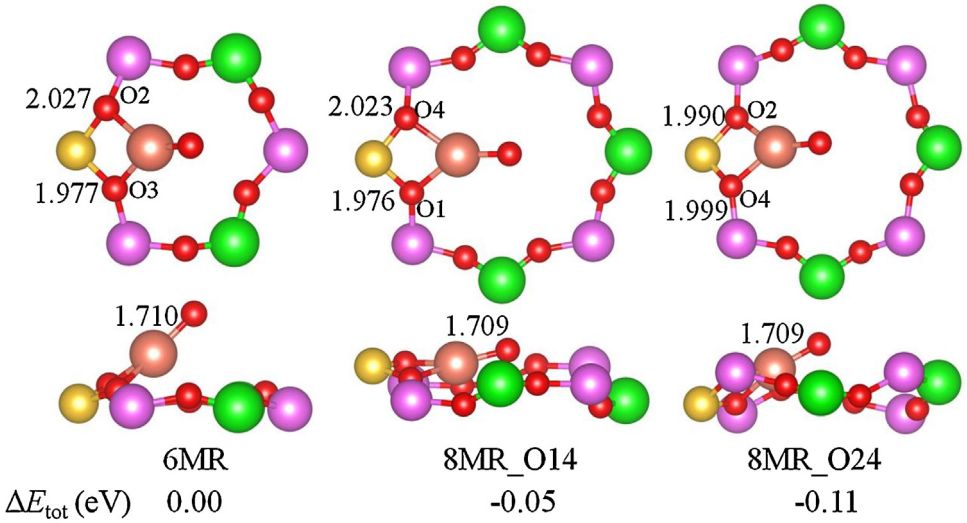

Fig. 5. Local structure of atomic O adsorbed ZCu with Cu in the 6MR, 8MR_O14, and 8MR_O24 sites. The color-coding for the spheres and the given distances have the same meaning as previous figures. The total energy differences with respect to the total energy of Cu in 6MR site (ΔE_{tot}) are given at the bottom of the figure.

Table 1
The calculated adsorption energies of H_2O, OH, O, O_2 and 2 OH on Cu in 6MR, 8MR_O14 and 8MR_O24 sites according to Eq. 2. The values of adsorption energy for 2 OH adsorbed ZCu is calculated by following the ZCuOH + OH → ZCu(OH)$_2$ process.

E_{ads} (eV)	6MR	8MR_O14	8MR_O24
O	0.45	−0.08	−0.21
O_2	−0.55	−1.09	−1.22
H_2O	−0.92	−1.64	−1.56
OH	−2.67	−3.17	−3.31
2 OH	−2.31	−1.69	−1.61

shown in Fig. 5, it is found that configurations of Cu in the 8MR sites become more favorable under O adsorption, although the energy difference is very small. This means that the thermodynamic stability of molecular species adsorbed in the ZCu conformation is nearly identical for Cu in different sites with the formation of a $[Cu^{2+}(O^-)]^+$ complex. As shown in Table 1, the calculated adsorption energies of O with respect to a O_2 molecule are 0.45, −0.08 and −0.21 eV for Cu in 6MR, 8MR_O14 and 8MR_O24 sites, respectively. The positive value of the adsorption energy of O on Cu in the 6MR site indicates that the adsorption of O is unfavorable. It also implies that the O_2 molecule does not prefer decomposing to two O atoms on Cu in the 6MR site. We next consider the molecular adsorption of an O_2 molecule at the Cu sites.

Previous computational results [40] have suggested that a side-on and an end-on configuration of O_2 with a triplet ground state to be favorable. It is reported that the side-on configuration is more favorable for O_2 adsorbed on Cu-SSZ-13 [40]. We studied both of these configurations on Cu in the three different sites and found that the end-on configuration is more favorable for O_2 adsorbed on ZCu. Initial structures of the side-on configuration automatically became an end-on configuration during the optimization. The optimized structures of end-on configuration for O_2 adsorption are shown in Fig. 6.

The O_2 molecule draws Cu somewhat less far out of the 6MR than does the O species. Upon the adsorption of an O_2 molecule, the Cu ion coordinates with two lattice O atoms and one O atom of the O_2 molecule. The adsorption of the O_2 molecule in the ZCu conformation also decreases the total energy difference between the 6MR and 8MR sites. Specifically, the total energy differences with respect to Cu in the 6MR are −0.05 and −0.12 eV for Cu in 8MR_O14 and 8MR_O24 sites, respectively. As listed in Table 1, the adsorption energies of O_2 on Cu in the 6MR, 8MR_O14 and 8MR_O24 sites are −0.55, −1.09 and −1.22 eV, respectively.

We investigated how an O_2 molecule could decompose, by examining the adsorption of 2 O atoms on a single Cu^+ ion. Because there is only one side for the molecule to access in the 6MR, we put 2 O atoms as far as possible from each other. The distance between the 2 O atoms was set to about 2.4 Å in the initial structure. How-

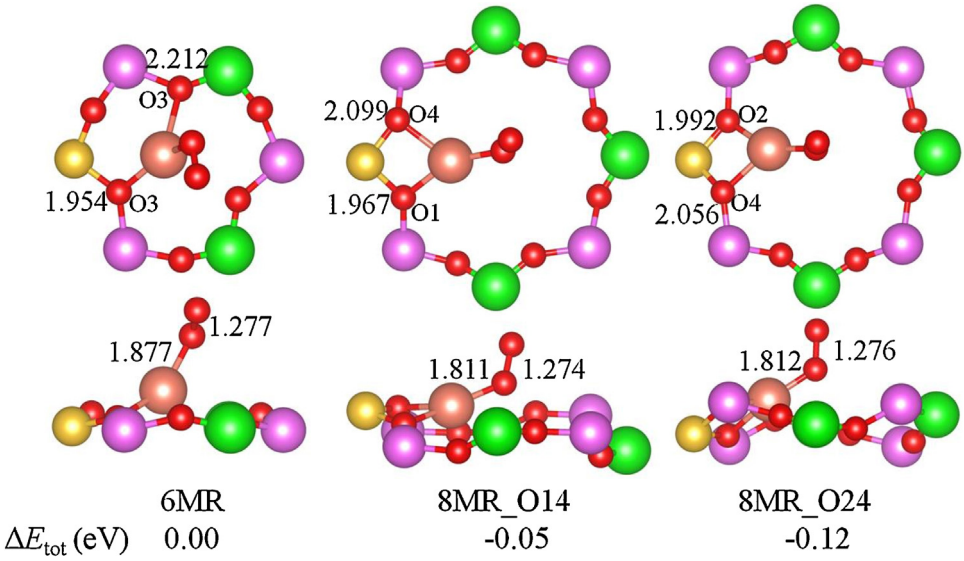

Fig. 6. Local structure of O_2 molecule adsorbed ZCu with Cu in the 6MR, 8MR_O14, and 8MR_O24 sites. The color coding for the spheres and the given distances have the same meaning as previous figures. The total energy differences with respect to the total energy of Cu in the 6MR site (ΔE_{tot}) are given at the bottom of the figure.

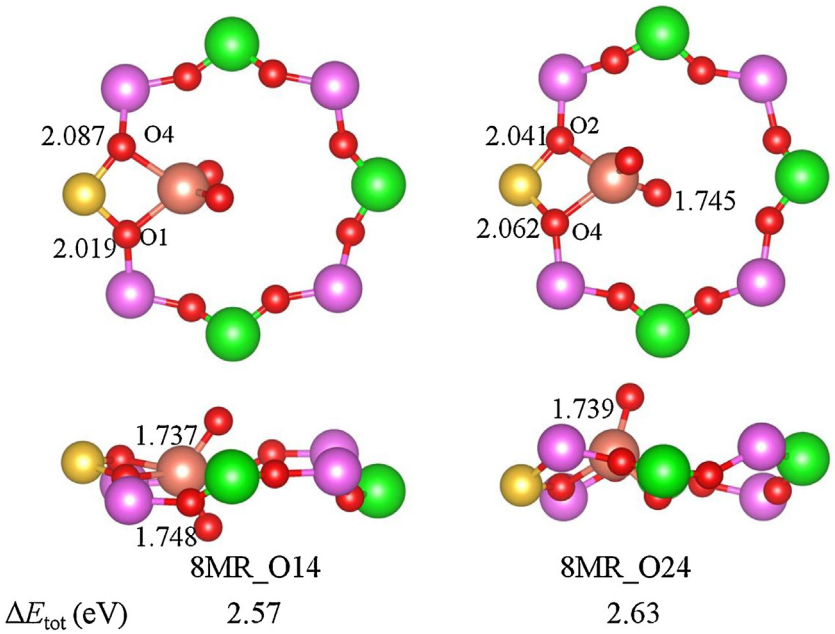

Fig. 7. Local structure of 2 O atoms adsorbed on a Cu^+ ion in the 8MR_O14 and 8MR_O24 sites. The color-coding for the spheres and the given distances have the same meaning as in the previous figures. ΔE_{tot} presents the total energy difference with respect to the corresponding configurations with an adsorbed O_2 molecule.

ever, after optimization, an O_2 molecule is formed on the Cu ion in the 6MR. This again confirms that an O_2 molecule will not dissociate when Cu is in a 6MR site. Different from the 6MR site, the 8MR has two sides that a molecule can access. As a result, the 2 O atoms can separately adsorb on both sides of the 8MR site. The optimized structures for Cu in 8MR_O14 and 8MR_O24 sites are shown in Fig. 7. Similar to the adsorption of an O atom and an O_2 molecule, the Cu ion approaches two lattice O atoms upon the adsorption of two extra-lattice oxygen atoms. As a result, the Cu ion becomes four-fold coordinated by oxygen. As presented in Fig. 7, the total energy differences with respect to the corresponding O_2 molecule adsorbed on a Cu^+ ion in the 8MR sites are 2.57 and 2.63 eV. These large positive values demonstrate that the decomposition of O_2 on a Cu^+ ion in either of the 8MR sites is thermodynamically unfavorable.

The interaction of H_2O with the Cu-SSZ-13 zeolite framework was also investigated theoretically for a variety of configurations [24,40]. Fig. 8 displays the optimized structure of H_2O adsorbed on Cu in different locations. For all considered Cu positions, Cu approaches one activated lattice O atom with a Cu—O bond length of 1.875, 1.919 and 1.885 Å for Cu in 6MR, 8MR_O14, and 8MR_O24 sites, respectively. Although H_2O draws Cu out of the 6MR plane, the H atom of H_2O tends to interact with a lattice O atom, where the distance between the H and O atoms is 1.795 Å. Similarly, when Cu is in one of the 8MR sites, the H atoms of H_2O interact with lattice O atoms, as shown in Fig. 8. The Cu coordination is 2-fold upon the adsorption of H_2O. The adsorption energies of H_2O on Cu in the 6MR, 8MR_O14, and 8MR_O24 sites are −0.92, −1.64 and −1.56 eV, respectively. It is found that H_2O has a stronger interaction with ZCu than the O atom or the O_2 molecule. Comparing

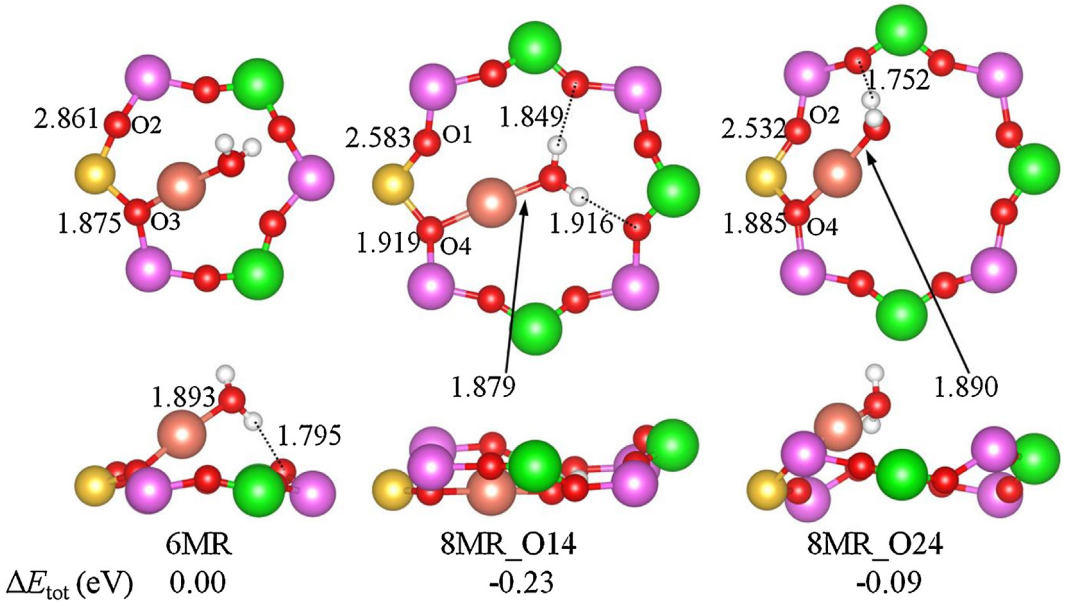

Fig. 8. Local structure of an H_2O molecule adsorbed on a Cu^+ ion in the 6MR, 8MR_O14, and 8MR_O24 sites. The color-coding for the spheres and the given distances have the same meaning as previous figures. The total energy differences with respect to the total energy of Cu in the 6MR site (ΔE_{tot}) are presented at the bottom of the figure.

the total energies of the three configurations, we find that H_2O stabilizes the 8MR_O14 configuration as compared to the 6MR sites with an energy difference of −0.23 eV with respect to the 6MR configuration.

Due to the deprotonation of H_2O, the OH species can also be adsorbed on a Cu site. As shown in Table 1, the adsorption energies of OH on Cu in the 6MR, 8MR_O14 and 8MR_O24 sites are −2.67, −3.17 and −3.31 eV, respectively. Note that the adsorption energy of OH was calculated by using the reference of neutral OH in the gas phase. OH presents a strong interaction with Cu because of its high activity. Fig. 9a shows the relaxed structure for the OH species adsorbed on Cu in the 6MR, 8MR_O14 and 8MR_O24 sites. Similar to the adsorption of the O atom, the adsorption of OH draws Cu out of the plane of the 6MR into a location above the 6MR. Upon OH adsorption, Cu is coordinated to the two activated O atoms and to the O of the OH adsorbate, which results in a net 3-fold coordination of Cu in each location. The Cu—O bond lengths of Cu with the lattice O atoms are about 2.0 Å while the bond distance between the Cu formed with extra-framework O atom of the OH adsorbate is about 1.8 Å. As for the total energy difference between these configurations, we find that the thermodynamic stability between the 8MR sites and the 6MR sites of the ZCu conformation in the presence of an OH adsorbate to be nearly identical.

We also considered the adsorption of a second OH species on such Cu sites, for which the relaxed structures are shown in Fig. 9b. The calculation for the adsorption of the second OH molecule follows the $ZCuOH + OH \rightarrow ZCu(OH)_2$ reaction pathway. The calculated adsorption energies are listed in Table 1. For Cu in the 6MR site, Cu is 4-fold coordinated, with two essentially equivalent short bonds to the OH molecule and two longer bonds to the lattice O. The adsorption energy of the second OH molecule is −2.31 eV for Cu in the 6MR site, which is slightly smaller than −2.67 eV for the first OH molecule. However, Cu in the 8MR sites exhibits a different behavior upon addition of a second OH. As shown in Fig. 9, it is found that the second OH molecule increases the distance between Cu and the O4 oxygen atom from 2.002 to 2.622 Å for the 8MR_O14 site and from 1.991 to 2.518 for the 8MR_O24 site, breaking the Cu-O4 bond. This results in a 3-fold coordinated Cu atom with two short bonds to the OH molecule and a longer bond length to the lattice O. The adsorption energies of the second OH molecule are −1.69 and −1.61 eV for Cu in 8MR_O14 and 8MR_O24 sites, respectively, which are just half of values for the adsorption energies of the first OH species (−3.17 and −3.31 eV). We can also examine the average adsorption energies of OH for 2 OH molecules adsorbed in the ZCu conformation using the following Eqs:

$$E_{ads}^{OH} = (E_{tot} - E_{ZCu} - 2E_{OH})/2 \quad (3)$$

where E_{tot}, E_{ZCu}, and E_{OH} are the total energies of ZCu upon the adsorption of 2 OH species, the clean ZCu conformation, and the isolated OH species in the gas phase, respectively. The calculated average adsorption energies are −2.49, −2.43 and −2.46 eV for Cu in the 6MR, 8MR_O14 and 8MR_O24 sites, respectively. It is concluded that, upon the adsorption of 2 OH species, the average adsorption energy of OH is close to that found for the adsorption of one OH species on Cu in the 6MR site (−2.67 eV). A similar comparison reveals that the interaction between OH and Cu is weaker for the adsorption of two OH species than for the adsorption of one OH species when Cu is in one of the 8MR sites (−3.17 and −3.31 eV for 8MR_O14 and 8MR_O24, respectively). In addition, the adsorption of the second OH makes the 6MR site more energetically favorable, as presented in Fig. 9b since this results in a positive value of total energy difference with respect to that of Cu in 6MR site (0.60 and 0.61 eV for the 8MR_O14 and 8MR_O24, respectively).

3.4. Phase diagram

The first principles phase diagram approach provides a connection between the DFT results and the relative equilibrium stabilities of the $ZCuO_xH_y$ species considered above [40]. A brief summary on how to construct the phase diagram is described here and detailed information can be found in the paper of McEwen et al. [40] The free energy of a ZCu with adsorbate, which is related to the adsorption energies, is written using the chemical potentials of oxygen and hydrogen:

$$\Delta G = G\left(ZCuO_xH_y\right) - G(ZCu) - x_O\mu_O - y_H\mu_H \quad (4)$$

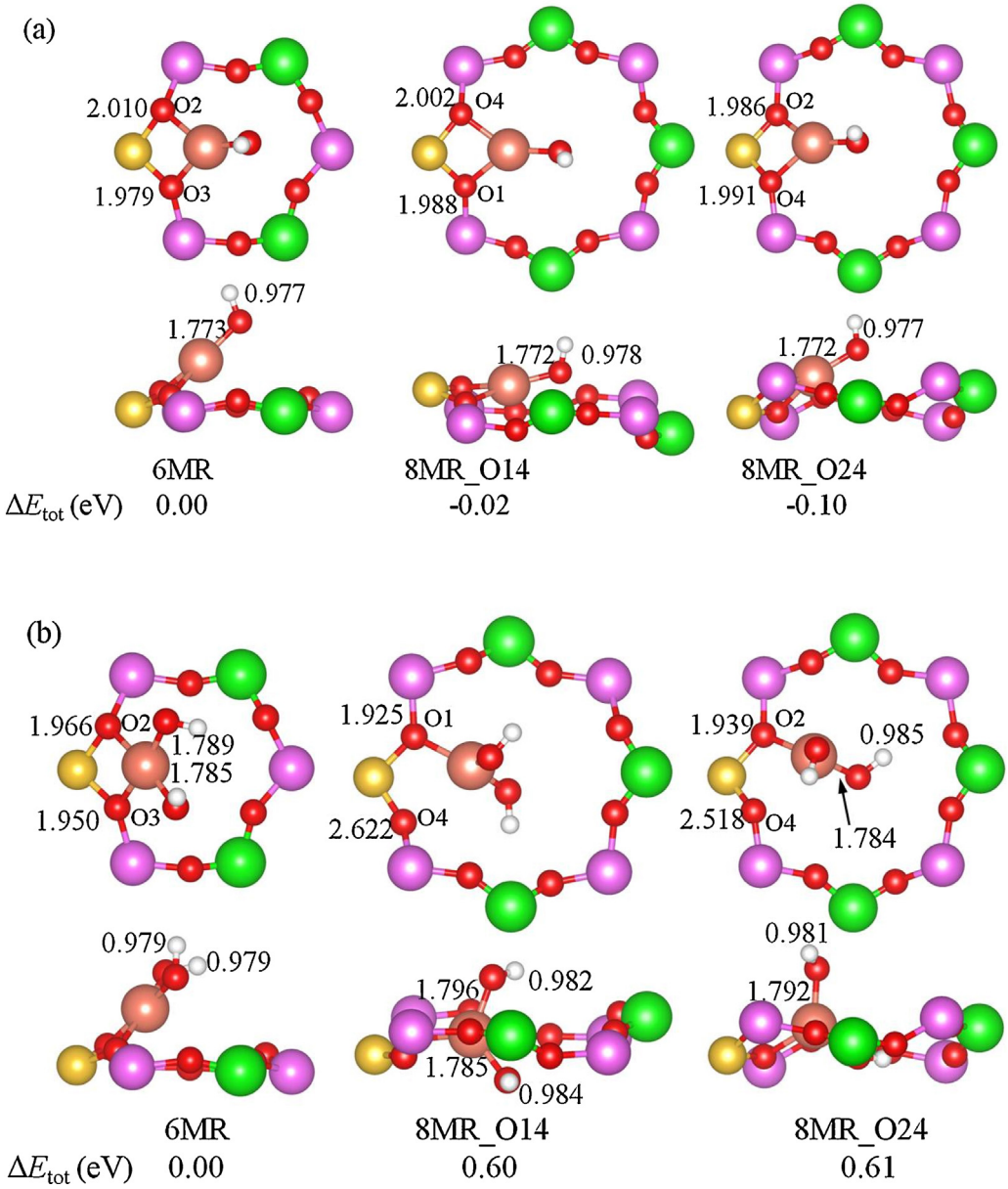

Fig. 9. Local structure of (a) OH and (b) 2 OH adsorbed in a ZCu conformation with Cu in the 6MR, 8MR_O14, and 8MR_O24 sites. The color coding for the spheres and the given distances have the same meaning as previous figures. The total energy differences with respect to the total energy of Cu in the 6MR site (ΔE_{tot}) are presented at the bottom of the figure.

The free energies of the zeolite species were approximated with the DFT energies. We take H_2O as the hydrogen reference to relate μ_H and μ_O:

$$\mu_H = \frac{1}{2}\left(\mu_{H_2O} - \mu_O\right) \tag{5}$$

Then Eq. (4) can be written as:

$$\Delta G = E(ZCuO_xH_y) - E(ZCu) - (x_O - \frac{y_H}{2})\mu_O - \frac{y_H}{2}\mu_{H_2O} \tag{6}$$

We define the relative chemical potential of oxygen and water with respect to the energies of isolated O_2 and H_2O molecules (E_{O_2} and E_{H_2O}) as reference zero:

$$\Delta\mu_O = \mu_O - \frac{E_{O_2}}{2} \text{ and } \Delta\mu_{H_2O} = \mu_{H_2O} - E_{H_2O} \tag{7}$$

As a result, Eq. (6) can be recast as a function of the relative chemical potential of oxygen and water:

$$\Delta G = E\left(ZCuO_xH_y\right) - E\left(ZCu\right) - \frac{1}{2}\left(x_O - \frac{y_H}{2}\right)E_{O_2} - \frac{1}{2}E_{H_2O} - \left(x_O - \frac{y_H}{2}\right)\Delta\mu_O - \frac{y_H}{2}\Delta\mu_{H_2O} \tag{8}$$

Other choices of chemical potential reference are possible. The chemical potentials can be related to temperature and gas pressure by using the ideal gas law. Detailed information can be found in the literature and its Supplementary Information [40].

Fig. 10a shows the computed relative free energies of Cu in a 6MR site as a function of the oxygen chemical potential. As described in Ref. [40], in order to understand the SCR reaction environment, the NO ⇔ NO_2 equilibrium over the catalyst surface can be assumed to obtain the chemical potential of oxygen, namely,

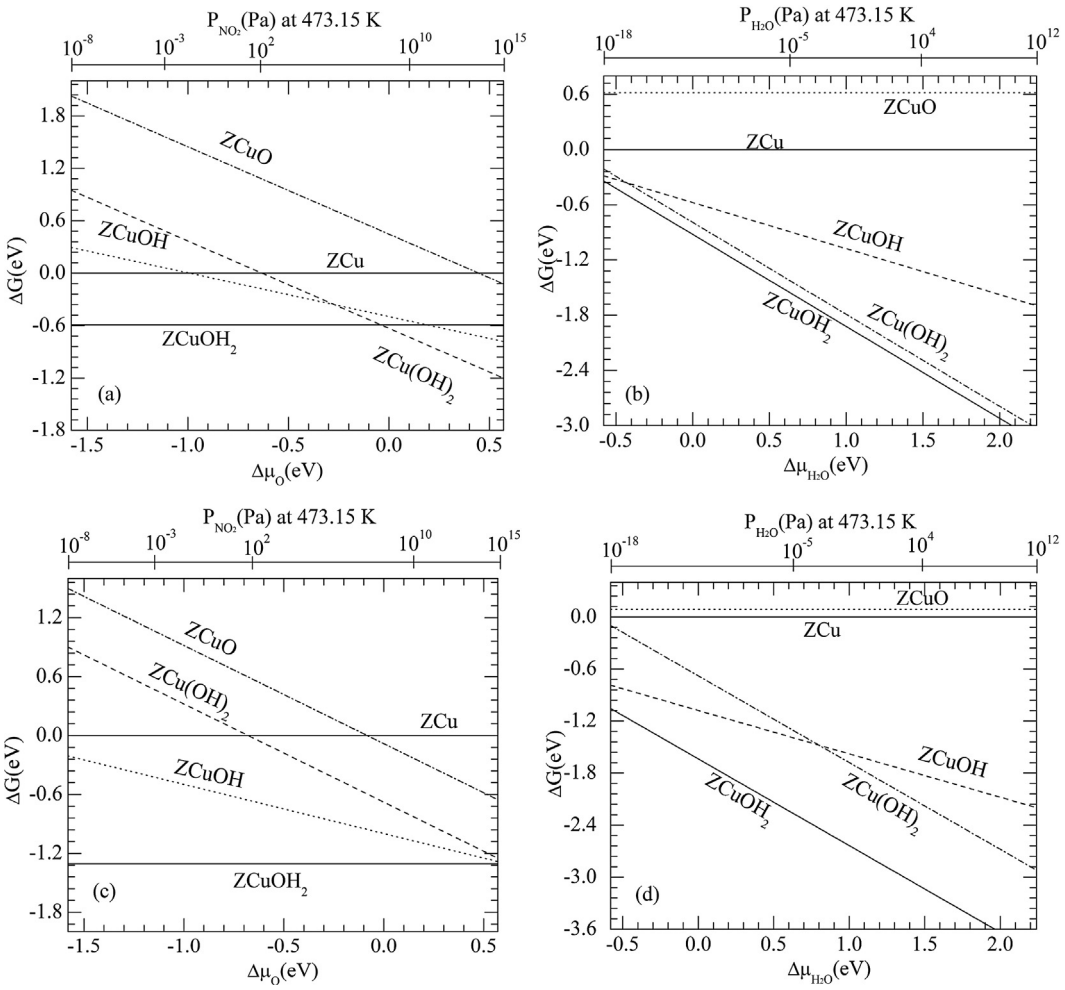

Fig. 10. The phase diagram comparing the relative stabilities of the configurations given in Figs. 4, 5, 8 and 9: phase diagram as a function of $\Delta\mu_O$ at p^{H_2O} = 0.1 bar and T = 473.15 K with Cu in (a) 6MR site and (c) 8MR_O14 site, phase diagram as a function of $\Delta\mu_{H_2O}$ at p^{O_2} = 0.05 bar and T = 473.15 K with Cu in (b) 6MR site and (d) 8MR_O14 site. The corresponding pressure scales are given in the figure. The left limit of the diagram corresponds to low NO_2 (H_2O) pressures or relatively reducing conditions.

$\mu_O = \mu_{NO_2} - \mu_{NO}$.Therefore, μ_O can be mapped to p^{NO_2} at a fixed p^{NO} O = 300 ppm at 473.15 K. μ_{H_2O} is determined at the condition of p^{H_2O} (473.15 K) = 0.1 bar. The calculated chemical potentials of H_2, O_2, H_2O, NO and NO_2 at different temperatures, which were used to obtain the chemical potential at any pressure, are listed in Table S1. The most stable species are at the bottom of the diagram and the less stable ones at increasingly higher free energy. For the location of 6MR site, a Cu^+ bound to a single H_2O is found to be the most stable species for low chemical potential values. With increasing O chemical potential, and increasing oxidizing conditions the more oxidized Cu species (ZCuO, ZCuOH and $ZCu(OH)_2$) drop in free energy relative the reduced species (ZCu and $ZCuOH_2$). Further increasing the chemical potential of oxygen, $ZCu(OH)_2$ becomes the most stable adsorption state. However, this transition occurs at much higher pressures when examining the phase diagram for Cu in the 8 membered ring as shown in Fig. 10c. This phase diagram for Cu-SAPO-34 is similar to that of Cu-SSZ-13 [40]. Fig. 10b shows the computed relative free energies of Cu sites as a function of water chemical potential at a fixed oxygen chemical potential. Here $ZCu(OH)_2$ is slightly less stable than $ZCuOH_2$, and $ZCuOH_2$ is the most stable species in the potential range studied. This result is similar with the Cu-SSZ-13 study, where the $ZCuOH_2$ was also found to be the most stable species within the chemical potential range studied [40]. However, as can be seen in Fig. 10d, when Cu is in the 8MR_O14 site, $ZCuOH_2$ was always found to be the most stable species within the chemical potential range studied whatever the oxygen chemical potential and water chemical potential. Note that the phase diagram for Cu in a 8MR_O24 is similar with Cu in a 8MRO_14 and detailed information can be found in Fig. S4 in Supplementary Information. As shown in Fig. 1, the standard SCR conditions are 300 ppm NO, 300 ppm NH_3, 5% O_2, 5% H_2O, 5% CO_2 and balance heat 200 °C (473.15 K). Similarly with the discussion in the literature [40], $\Delta\mu_O$ corresponds approximately to −0.55 eV in Fig. 10a and c at p^{NO_2} (473.15 K) = 1000 pm and p^{NO} = 300 ppm. Under this condition of O chemical potential, the most stable species is $ZCuOH_2$.

3.5. Computational Cu K-edge XANES

3.5.1. Analysis of the XANES spectra of a clean Cu ion in Cu-SAPO-34

A XANES spectrum can provide information about the chemical environment of a species and can be used as a fingerprint for identification of a species. Differences in the Cu K-edge XANES spectra can be interpreted by comparing them to the excited 4*p* PDOS of Cu within the empty band region, as shown in Fig. 11. The 1*s*–4*s* and 1*s*–3*d* transitions are forbidden from the dipole selection rules and are not included in Fig. 11a. The 4*p* PDOS energy has been shifted according to the Fermi level of Cu to allow for direct comparison between the XANES spectra and the PDOS. For the three Cu locations (6MR, 8MR_O14 and 8MR_O24), as shown in Fig. 11a, there is an energy gap in the 4*p* states between the small peak around 8980 eV and the main peak around 8984 eV. We observe differences

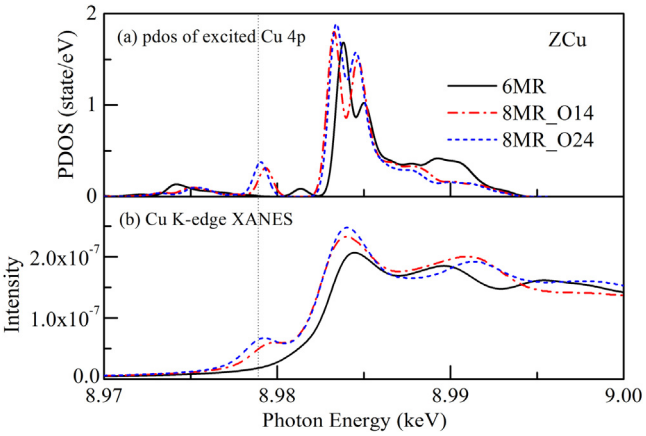

Fig. 11. The calculated PDOS of the excited Cu 4*p* state (a) and the computational K-edge XANES of Cu (b) in the 6MR (solid line), 8MR_O14 (dash-dotted line) and 8MR_O24 (dashed line) locations for clean ZCu. The vertical dashed line at 8978.9 eV shows the Fermi level.

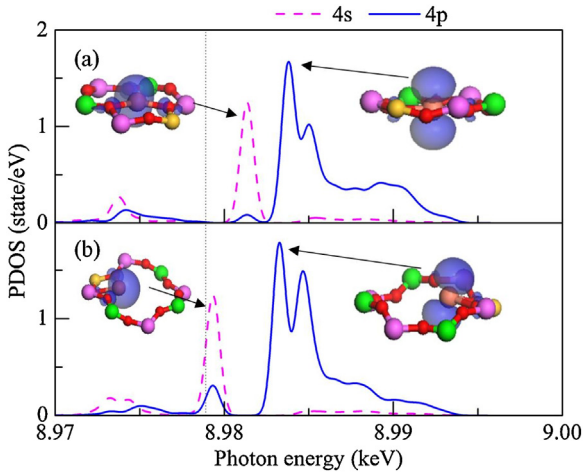

Fig. 12. The excited Cu ion orbital distributions in the (a) 6MR and (b) 8MR_O14 sites. We plotted the PDOS of 4*s* (dashed line) and 4*p* (dotted line) states because the orbital distribution cannot be separated by each state. The iso-surface value is 0.04 electrons/Å^3. The vertical dashed line at 8978.9 eV represents the Fermi level. The results for Cu in 8MR_O24 is similar with Cu in 8MR_O14 and detailed information can be found in Fig. S6 in Supplementary Information.

between the 4*p* states for Cu in the 8MR sites as compared to the 4*p* state for Cu in the 6MR site. The energy gap between the small peak and the main peak is larger for the 8MR conformations as compared to Cu in the 6MR. In addition, the intensity of the small peak for the 4*p* PDOS for Cu in 8MR sites is stronger than for Cu in the 6MR site. As discussed in our previous work with SSZ-13 [24], we conclude that the presence of the small peak feature around 8980 eV results from 1*s* to 4*p* transition when Cu is situated at one of the 8MR sites and that this feature is not present when Cu is in the 6MR site due to the smaller intensity of the 4*p* state in that energy range. As mentioned before, the coordination number of Cu in the 8MR_O14 and the 8MR_O24 sites is 2, as shown in Fig. 4. The fact that there is no big difference between the XANES of Cu in 8MR_O14 and 8MR_O24 sites implies that the XANES of Cu in 8MR_O14 site is independent on the longer Cu—O distance of 2.353 Å.

We analyzed the different peaks for the 4*p* PDOS of Cu in the 6MR and the 8MR sites by examining the orbital distributions, as displayed in Fig. 12. We confirmed that Cu in a 4*p* state, with the orbital distribution shown in Fig. 12 being a $4p_z$ orbital, mainly contributes the main peak around 8984 eV. However, the orbital distribution around 8982 eV for Cu in the 6MR contributed mainly

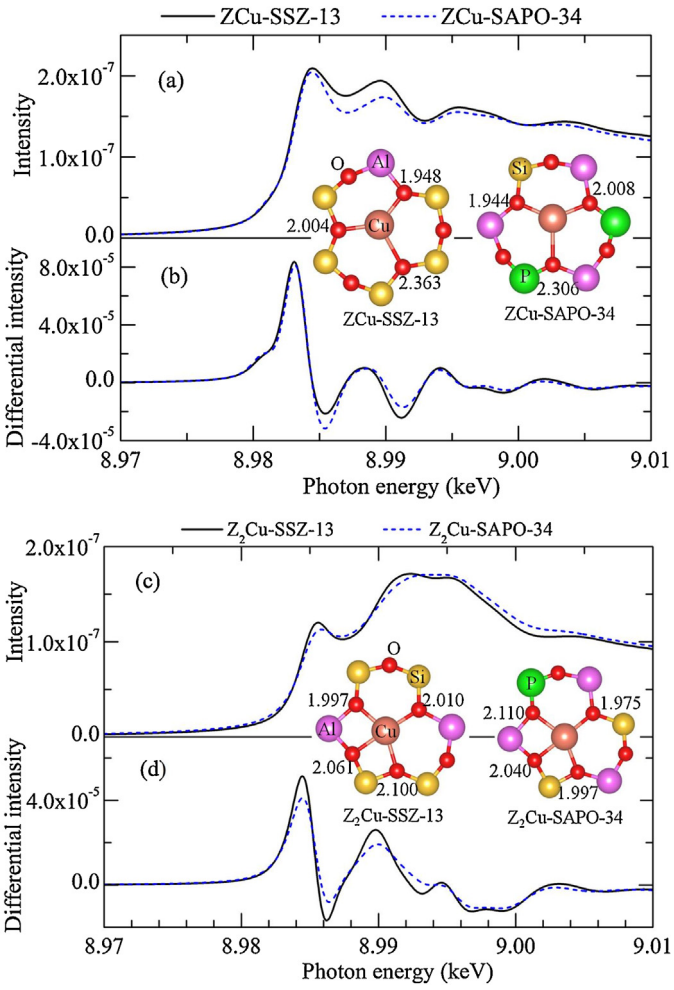

Fig. 13. Comparison of the Cu-SSZ-13 (solid line) and Cu-SAPO-34 (dashed line) XANES, with Cu in a (a) Cu^+ (ZCu) or in a (c) Cu^{2+} (Z_2Cu) oxidation state. The Cu ions are located in the 6MR site. The differential plots of the corresponding XANES are displayed in (b) Cu^+ and (d) Cu^{2+}, respectively. The local structures of Cu ions are shown in insert figure, as well as the distances between Cu ions and lattice O atoms.

to the 4*s* state with a small contribution from the 4*p* state. For Cu in one of the 8MR sites this combined contribution by both the 4*s* and 4*p* states is near the Fermi level. The different contributions of the 4*p* state for Cu in the 6MR and the 8MR sites result in a different shape of the orbital, as shown on the left of Fig. 12. Specifically, the Cu ion in the 6MR is centered in the orbital, while the Cu ion is located toward the edge of the orbital for Cu in 8MR. The orbital distribution of Cu in the 6MR is more symmetrical than that of Cu in the 8MR.

3.5.2. *XANES comparison of Cu-SSZ-13 and Cu-SAPO-34 in the absence of adsorbates*

Fig. 13 shows a comparison between the XANES of a clean Cu-SSZ-13 and Cu-SAPO-34, including both the Cu^+ and Cu^{2+} oxidation states. For the Cu^+ species, the coordination number is 3 for both Cu-SSZ-13 and Cu-SAPO-34. The distances between Cu and lattice O atoms are almost the same, respectively 1.948, 2.004, 2.363 Å and 1.944, 2.008, 2.306 Å for Cu-SSZ-13 and Cu-SAPO-34. The same oxidation state of 1+ and same local structure produce nearly identical Cu K-edge XANES for Cu-SSZ-13 and Cu-SAPO-34, as shown in Fig. 13a. The edge position is defined as the maximum of the differential plot of the rising edge in the XANES. Fig. 13b shows the differential plots of the Cu K-edge XANES for Cu^+-SSZ-13 and Cu^+-SAPO-34. It is found that the edge position of Cu^+ species in

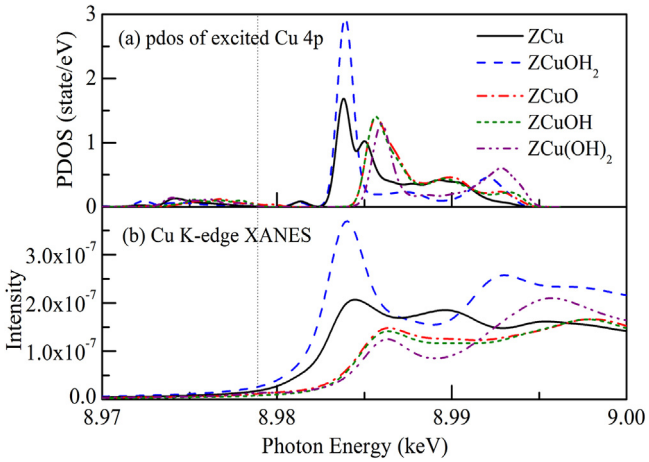

Fig. 14. (a) The excited 4*p* PDOS of Cu in the ZCu conformation in the presence of adsorbates (H_2O, O atom, OH and 2 OH with different oxidizing power. The Cu^+ ion is located in the 6MR site. (b) The corresponding K-edge XANES. The vertical dashed line at 8978.9 eV shows the Fermi level.

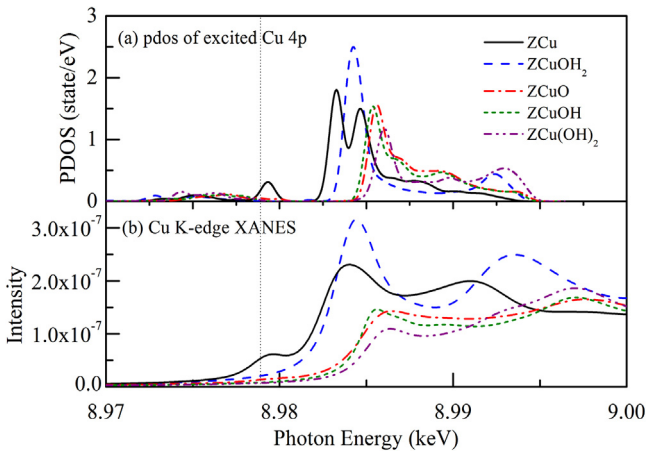

Fig. 15. (a) The excited 4*p* PDOS of Cu in the ZCu conformation in the presence of adsorbates (H_2O, O atom, OH and 2 OH) with different oxidizing power. Cu is located in 8MR_O14 site. (b) The corresponding K-edge XANES. The vertical dashed line at 8978.9 eV shows the Fermi level.

Table 2
Edge position shifts in the Cu K-edge XANES in the presence of several adsorbates in the ZCu conformation (as shown in Figs. 14 and 15, as well as in Fig. S7) with respect to the corresponding clean ZCu conformation with different Cu locations. The original data of the edge positions can be found in Table S1 of Supplementary Information. The resolution of the computational XANES is 0.05 eV.

Shift of edge position (eV)	Clean	H_2O	O	OH^-	$2OH^-$
6MR	0.00	−0.10[a]	1.75	1.67	1.94
8MR_O14	0.00	0.89	2.50	2.11	3.03
8MR_O24	0.00	0.14	2.30	1.67	2.93

[a] Note that for Cu in the 6MR site, Fig. 16 shows that the Cu edge position in the ZCu conformation in the presence of H_2O seems to be at a lower energy than that of the clean ZCu conformation. This is confirmed by the edge position shift.

clean Cu/CHA zeolite is located at the photon energy position of 8983.1 eV. A similar analysis can be applied when comparing the Z_2Cu conformations in Cu-SSZ-13 and Cu-SAPO-34, as shown in Fig. 13c. In such Z_2Cu conformations, we have replaced two Si atoms for two Al atoms (SSZ-13) or two P atoms for two Si atoms (SAPO-34). Different from the Cu^+ ion, the Cu^{2+} ion has a coordination number of 4. The edge position of the Cu^{2+} species in the clean Cu/CHA zeolite is located at a photon energy position of 8984.4 eV, which is higher than the Cu^+ species edge position with a difference of 1.3 eV. This result again confirms the trend of the edge shift with its oxidation state. As is well-known, the XANES is determined by the local structure and oxidation state of the exchanged Cu ion. However, it is not intuitive that a ring made from Al and Si atoms (Cu-SSZ-13) or Al, Si and P atoms (Cu-SAPO-34) can give us virtually identical XANES. Indeed, based on our analysis, even though we have completely different atoms making up the ring structures (Cu-SSZ-13 and Cu-SAPO-34), the XANES of Cu with a certain oxidation state would be hard to differentiate experimentally.

3.5.3. *Influence of adsorbates on the Cu K-edge spectra*

We chose several species (H_2O, O, OH and 2 OH) with different oxidizing powers to examine the relationship between the oxidizing power and the edge position. Figs. 14 and 15 display the XANES results for Cu in the 6MR and 8MR_O14 sites, respectively. Because the results are very similar for Cu in the 8MR_O14 and 8MR_O24 sites, the corresponding XANES and PDOS results are shown in Fig. S7 in Supplementary Information. The edge position shifts are listed in Table 2 for Cu in the 6MR, 8MR_O14 and 8MR_O24 sites. We can also interpret the XANES of Cu for each of these adsorbates through the corresponding excited 4*p* PDOS. For the 6MR conformation, Fig. 14a shows the excited 4*p* state for Cu as influenced by each of the adsorbates and Fig. 14b shows the corresponding XANES. As can be seen in Fig. 14b, the peak intensity of the Cu K-edge XANES is intensified when H_2O is adsorbed on the Cu, but this peak intensification does not occur with other adsorbates. Such a high peak intensity might be due to the interaction of the H atoms with lattice O atoms. Also observed in Fig. 14b, the edge positions varies noticeably in the presence of different adsorbing species. The edge position is defined as the maximum of the differential plot of the rising edge in the XANES. Overall, one can see in Fig. 14b that, with the exception of H_2O, the molecular adsorption of these adsorbates results in a shift of the edge position to higher energy. The XANES edge shifts for different molecules adsorbed on a Cu^+ ion with respect to corresponding clean ZCu conformation are listed in Table 2. It is found that the edge position and the oxidizing power are in the same order, namely clean Cu ≈ H_2O < O ≈ OH < 2 (OH) (from low to high energy). As is well-known, one would expect the higher edge position due to the higher binding energy of electrons in a Cu ion with a higher oxidation state. It is concluded that our computational XANES results capture the real trend of the edge shift with oxidation state. While the XANES discussion so far has focused on the situation of Cu in the 6MR site, we arrive at similar conclusions when Cu is located in the two 8MR sites as discussed below. Likewise, a similar conclusion was made in our previous work on the Cu-SSZ-13 zeolite [24].

The Cu K-edge XANES for the plot shown in Fig. 14b, with Cu in the 6MR site, is produced through an excitation of a 1*s* electron to the 4*p* state. This is illustrated by the projected density of states of the copper ion for the various adsorbates shown in Fig. 14a. Transition to another *s* state is dipole forbidden, and *s*- *d*-state transitions are highly unlikely [41]. The clean ZCu and the H_2O adsorbed ZCu conformations have 4*p* states at about the same energy level. The same trend toward higher energies observed in the XANES spectra is also seen in the *p*-states of Cu for each of the adsorbates.

Differently with Cu in 6MR site, the Cu K-edge XANES for Cu in the 8MR (8MR_O14) is shown in Fig. 15. The edge position for Cu in the 8MR follows a trend similar to Cu in the 6MR. For Cu in the 8MR, adsorption of H_2O results in a slightly higher energy of the edge position, indicating that H_2O has a slight oxidizing effect on Cu in the 8MR.

3.5.4. *Comparison of the XANES spectra with experiment*

Based on the construction of the phase diagram in Section 3.4, we have selected the most favorable conformations and compared them to the experimental XANES of Cu-SAPO-34. Such a compari-

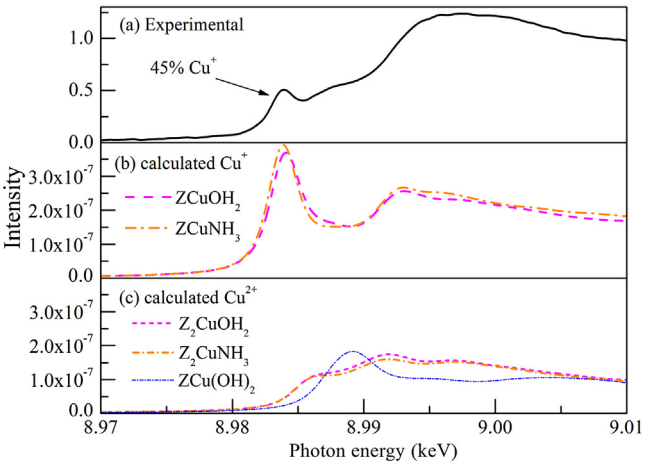

Fig. 16. (a) Experimental XANES spectrum of a commercial ~1.75 wt% Cu-SAPO-34 catalyst collected *operando* under standard SCR conditions [25]. Computational XANES for (b) Cu^+ and (c) Cu^{2+} species, where Cu is located in 6MR site. The atomic structures of $ZCuNH_3$, $ZCuOH_2$ and Z_2CuNH_3 can be found in Fig. S5 of the Supplementary Information.

son procedure of our theoretical K-edge XANES to the experimental results has been detailed in our previous work [24]. However, the construction of the phase diagram does not take into account the possible interaction of Cu exchanged ion with ammonia, which may block the adsorption of H_2O because the binding preference for NH_3 over H_2O in Cu-SSZ-13 [42]. As a result, we compare the XANES spectrum of Cu^{2+} and Cu^+ ions in the presence of NH_3 in addition to those considered in the construction of the phase diagram since ammonia is an important reactant. We also consider the interaction of water with a Cu^{2+} ion (Z_2CuOH_2) that has been charged compensated by two Al atoms, which has been shown to be a favorable configuration in the Cu-SSZ-13 system [40]. These additional conformations considered in this section are shown in Fig. S5 of Supplementary Information.

In Fig. 16, we show the experimental XANES spectra. As shown in Fig. 16a, it was determined that as much as 45% of the total Cu ions were Cu^+ under these conditions, where the photon energy of the Cu^+ peak is around 8984 eV. Details of the experimental procedure and quantification of the Cu^+ can be found elsewhere [25]. Using our computational results of the Cu K-edge XANES for Cu-SAPO-34 under different situations, we correlated the XANES of various model species to the experimental XANES collected *operando* under standard SCR conditions. We compare the experimentally assigned Cu^+ peak, with our $ZCuOH_2$ model in Fig. 16, which was determined to be the most energetically favorable configuration for a wide range of oxygen and water chemical potential values. We also compare the XANES spectrum of an NH_3 molecule bonded to a Cu ion in the ZCu conformation, which we denote as a $ZCuNH_3$ configuration. The calculated photon energy distribution of the Cu^+ peaks of H_2O and NH_3 adsorbed ZCu correlate well with the experimental XANES in the same photon energy range, as shown in Fig. 11b. Interestingly, the XANES spectrum of the $ZCuOH_2$ and $ZCuNH_3$ conformations are very similar, so it would be hard to distinguish the presence of both species based on the XANES their respective XANES spectra alone.

We also found in the construction of the phase diagram that under oxidizing conditions that the $ZCu(OH)_2$ species becomes increasingly more energetically favorable. By examining the XANES of the Cu^{2+} species, as shown in Fig. 11c, we find that the middle peak of the experimental XANES spectrum at 8988 eV corresponds well to the peak found for the $ZCu(OH)_2$ species. The XANES spectrum for the other species considered ($ZCuOH_2$ and $ZCuNH_3$) correlate well with the highest energy peak of the XANES spectrum at around 8995 eV. It is also interesting to see that the XANES spectra for Z_2CuOH_2 and Z_2CuNH_3 are very similar, as was the case when comparing the XANES spectra for the $ZCuOH_2$ and the $ZCuNH_3$ conformations. However, it is found that the peak intensities of the Cu^{2+} species in the presence of ammonia and water are much lower than those for a Cu^+ ion in the presence of water or ammonia in a ZCu conformation, as can be seen when comparing Fig. 16b and c.

4. Conclusions

In summary, through calculations from first principles, the properties of Cu-SAPO-34 were studied at the atomic level. For pure SSZ-13 and ALPO-34, the equilibrium volume of ALPO-34 is larger than that of SSZ-13, which is a result of the shorter average bond lengths between the tetrahedral sites on the lattice oxygen atoms for SSZ-13 (1.625 Å) as compared to the corresponding ones for ALPO-34 (1.645 Å). Similar to the ZCu conformation in Cu-SSZ-13, it is found that the 6MR site is the most energetically favorable site as compared to the 8MR sites with total energy differences in Cu-SAPO-34 of about 0.5 eV with respect to the 6MR site. In addition, the Cu binding energies were found to be −0.88, −0.38 and −0.32 eV for Cu in the 6MR, 8MR_O14 and 8MR_O24 sites, respectively. Upon the adsorption of the species (H_2O, O, OH and 2OH) we studied in this contribution, the energy differences between Cu in the 8MR and 6MR sites decreases and almost disappears, which means that the thermodynamic stability of Cu becomes nearly identical in different locations. It is also found that the decomposition of O_2 on Cu ions is thermodynamically unfavorable. By comparing the average adsorption energies per molecule of OH and 2 OH species on a Cu^+ ion, we concluded that upon the adsorption of 2 OH species, the average interaction between OH and the Cu^+ ion is close to that found with the adsorption of one OH species on a Cu^+ ion in the 6MR, however the average adsorption energy is weaker than the adsorption of a single OH species when Cu is in one of the 8MR sites. Further, a thermodynamic phase diagram study showed that for the ZCu conformation in Cu-SAPO-34, at a given chemical potential of H_2O, Cu^+ bound to a single H_2O is found to be the most stable species at low oxygen potential values while the ZCu conformation in Cu-SAPO-34 with the adsorption of 2 OH species is the most stable at high oxygen chemical potential values.

The X-ray absorption near edge structure (XANES) of Cu in Cu-SAPO-34 under different conditions was also modeled from first principles. An excellent correlation was found between the excited 4*p* PDOS of Cu and the K-edge XANES. By comparing the Cu K-edge XANES between Cu-SSZ-13 and Cu-SAPO-34 with Cu in a +1 or +2 oxidation state, we concluded that even though we have completely different atoms making up the structures (Cu-SSZ-13 and Cu-SAPO-34), the XANES of Cu with certain oxidation state is hard to differentiate. As is well-known, one would expect the higher edge position to be due to the higher binding energy of electrons in a higher oxidation state. By studying the Cu K-edge XANES of Cu-SAPO-34 with the adsorption of species of different oxidizing power, it is concluded that our computational XANES results capture the real trends of the edge shift with oxidation state. Finally, we were able to gain a number of insights into the experimental XANES spectrum under standard SCR conditions by comparing it to the simulated XANES spectrum of several favorable conformations determined in part from the construction of the phase diagram. We found the $ZCuOH_2$ and the $ZCuNH_3$ conformations correlated well with the experimental Cu^+ peak region. On the other hand, the simulated XANES for the Z_2CuOH_2, Z_2CuNH_3 and $ZCu(OH)_2$ conformations correlated well with the experimental Cu^{2+} peak regions of the XANES spectrum.

Acknowledgements

This work was supported by institutional funds provided to JSM from the Voiland School of Chemical Engineering and Bioengineering and was partially funded by USDA/NIFA through Hatch Project #WNP00807 titled: "Fundamental and Applied Chemical and Biological Catalysts to Minimize Climate Change, Create a Sustainable Energy Future, and Provide a Safer Food Supply". Financial support was also provided by the National Science Foundation GOALI program under contract No. CBET-1258717. We thank Prof. Fabio Ribeiro for the experimental XANES data. We also thank Mr. Atish Parekh, Prof. W. F. Schneider, Mr. Christopher Paolucci, Mr. Trunjoyo Anggara, Dr. Chuck Peden and Prof. Jeff Miller for stimulating discussions on the modeling and Ms. Alyssa Hensley for her comments on the manuscript. A portion of the computer time for the computational work was performed using EMSL, a national scientific user facility sponsored by the Department of Energy's Office of Biological and Environmental Research and located at PNNL. PNNL is a multi-program national laboratory operated for the US DOE by Battelle. K.H., Seattle Chapter ARCS Fellow, gratefully acknowledges financial support from the Achievement Rewards for College Scientists foundation.

Appendix A. Supplementary data

Supplementary data associated with this article can be found, in the online version, at http://dx.doi.org/10.1016/j.cattod.2016.01.025.

References

[1] S.J. Schmieg, S.H. Oh, C.H. Kim, D.B. Brown, J.H. Lee, C.H.F. Peden, D.H. Kim, Catal. Today 184 (2012) 252.
[2] D.W. Fickel, E. D'Addio, J.A. Lauterbach, R.F. Lobo, Appl. Catal. B 102 (2011) 441.
[3] J. Xue, X. Wang, G. Qi, J. Wang, M. Shen, W. Li, J. Catal. 297 (2013) 56.
[4] F. Gao, E.D. Walter, N.M. Washton, J. Szanyi, C.H.F. Peden, ACS Catal. 3 (2013) 2083.
[5] T. Yu, D. Fan, T. Hao, J. Wang, M. Shen, W. Li, Chem. Eng. J 243 (2014) 159.
[6] L. Ma, Y. Cheng, G. Cavataio, R.W. McCabe, L. Fu, J. Li, Chem. Eng. J. 225 (2013) 323.
[7] P.N.R. Vennestrøm, A. Katerinopoulou, R.R. Tiruvalam, A. Kustov, P.G. Moses, P. Concepcion, A. Corma, ACS Catal. 3 (2013) 2158.
[8] D. Wang, Y. Jangjou, Y. Liu, M.K. Sharma, J. Luo, J. Li, K. Kamasamudram, W.S. Epling, Appl. Catal. B 165 (2015) 438.
[9] D. Wang, L. Zhang, J. Li, K. Kamasamudram, W.S. Epling, Catal. Today 231 (2014) 64.
[10] T. Yu, T. Hao, D. Fan, J. Wang, M. Shen, W. Li, J. Phys. Chem. C 118 (2014) 6565.
[11] L. Wang, W. Li, G. Qi, D. Weng, J. Catal. 289 (2012) 21.
[12] J. Xue, X. Wang, G. Qi, J. Wang, M. Shen, W. Li, J. Catal. 297 (2013) 56.
[13] A.A. Verma, S.A. Bates, T. Anggara, C. Paolucci, A.A. Parekh, K. Kamasamudram, A. Yezerets, J.T. Miller, W.N. Delgas, W.F. Schneider, F.H. Ribeiro, J. Catal. 312 (2014) 179.
[14] J. Wang, Y. Huang, T. Yu, S. Zhu, M. Shen, W. Li, J. Wang, Catal. Sci. Technol. 4 (2014) 3004.
[15] F. Gao, J. Kwak, J. Szanyi, C.F. Peden, Top. Catal. 56 (2013) 1441.
[16] D. Wang, L. Zhang, K. Kamasamudram, W.S. Epling, ACS Catal. 3 (2013) 871.
[17] L. Ma, Y. Cheng, G. Cavataio, R.W. McCabe, L. Fu, J. Li, Appl. Catal. B 156–157 (2014) 428.
[18] S.Y. Joshi, A. Kumar, J. Luo, K. Kamasamudram, N.W. Currier, A. Yezerets, Appl. Catal. B 165 (2015) 27.
[19] E.L. Uzunova, H. Mikosch, J. Hafner, J. Phys. Chem. C 112 (2008) 2632.
[20] E.L. Uzunova, F. Göltl, G. Kresse, J.r. Hafner, J. Phys. Chem. C 113 (2009) 5274.
[21] E.L. Uzunova, H. Mikosch, J. Hafner, J. Mol. Struct.: THEOCHEM 912 (2009) 88.
[22] E.L. Uzunova, H. Mikosch, G. St Nikolov, Int. J. Quantum Chem. 113 (2013) 723.
[23] R. Zhang, J.-S. McEwen, M. Kollár, F. Gao, Y. Wang, J. Szanyi, C.H.F. Peden, ACS Catal. 4 (2014) 4093.
[24] R. Zhang, J. Szanyi, F. Gao, J.-S. McEwen, Catal. Sci. Technol. (2016), http://dx.doi.org/10.1039/C5CY02252E.
[25] V.F. Kispersky, A.J. Kropf, F.H. Ribeiro, J.T. Miller, Phys. Chem. Chem. Phys. 14 (2012) 2229.
[26] G. Kresse, J. Furthmüller, Phys. Rev. B 54 (1996) 11169.
[27] G. Kresse, J. Hafner, Phys. Rev. B 47 (1993) 558.
[28] P.E. Blöchl, Phys. Rev. B 50 (1994) 17953.
[29] G. Kresse, D. Joubert, Phys. Rev. B 59 (1999) 1758.
[30] J.P. Perdew, Y. Wang, Phys. Rev. B 45 (1992) 13244.
[31] Y. Jeanvoine, J.G. Ángyán, G. Kresse, J. Hafner, J. Phys. Chem. B 102 (1998) 5573.
[32] F. Göltl, P. Sautet, J. Chem. Phys. 140 (2014) 154105.
[33] S.J. Clark, M.D. Segall, C.J. Pickard, P.J. Hasnip, M.J. Probert, K. Refson, M.C. Payne, Z J. Krist. 20 (2005) 567.
[34] S.-P. Gao, J.P. Chris, P. Alexander, M. Victor, J. Phys. Conden. Matter. 21 (2009) 104203.
[35] J.P. Perdew, K. Burke, M. Ernzerhof, Phys. Rev. Lett 77 (1996) 3865.
[36] S.-P. Gao, C.J. Pickard, M.C. Payne, J. Zhu, J. Yuan, Phys. Rev. B 77 (2008) 115122.
[37] V. Milman, K. Refson, S.J. Clark, C.J. Pickard, J.R. Yates, S.P. Gao, P.J. Hasnip, M.I.J. Probert, A. Perlov, M.D. Segall, J. Mol. Struct.: THEOCHEM 954 (2010) 22.
[38] T. Fjermestad, S. Svelle, O. Swang, J. Phys. Chem. C 117 (2013) 13442.
[39] F. Gao, E.D. Walter, N.M. Washton, J. Szanyi, C.H.F. Peden, Appl. Catal. B 162 (2015) 501.
[40] J.S. McEwen, T. Anggara, W.F. Schneider, V.F. Kispersky, J.T. Miller, W.N. Delgass, F.H. Ribeiro, Catal. Today 184 (2012) 129.
[41] T. Yamamoto, X-Ray Spectrom. 37 (2008) 572.
[42] C. Paolucci, A.A. Verma, S.A. Bates, V.F. Kispersky, J.T. Miller, R. Gounder, W.N. Delgass, F.H. Ribeiro, W.F. Schneider, Angew. Chem. Int. Ed. 53 (2014) 11828.